# Direct dating Paleo-fluid flow events in sedimentary basins

Peng Yang[1], Keyu Liu[1], Zhen Li[2], Kai Rankenburg[2], Brent I.A. McInnes[3], Jianliang Liu[1], and Noreen J. Evans[3]

[1]China University of Petroleum (East China)
[2]Curtin University
[3]School of Earth and Planetary Science, Curtin University

November 22, 2022

## Abstract

Reconstructing fluid evolution history in old sedimentary basins is extremely challenging due to the prolonged evolution, lack of exact age constraints and absence of preserved fluids. By integrating *in-situ* calcite U-Pb dating, fluid inclusion analysis, and high-resolution measurements of carbon-oxygen-strontium isotopes and rare earth elements (REEs), we have reconstructed the fluid evolution history in an Ordovician deeply-buried carbonate reservoir in the Tarim Basin, China with unprecedented temporal resolution. Five generations of calcite cementation spanning over 37 m.y. are dated in a single calcite vein with U-Pb ages ranging from ~353 Ma to ~316 Ma. The initial cement was associated with an intrusion of hyper-saline brine enriched REEs. This was followed by influx of meteoric water to precipitate the second and third generations of cement, characterized by a reduced salinity, anomalously high Sr isotopic ratios and extremely low concentrations of REEs. The fourth generation of cement was formed in a deep-fluid system accompanied by oil charge as indicated by the presence of bitumen, oil inclusions and lighter C and Sr isotope ratios. The fifth generation of cement was precipitated from an equilibrated connate water, having the lowest salinity and a comparable REE signature with the host rock. Oil charge was dated to be around 326 Ma. This study demonstrates the effectiveness in combining *in-situ* calcite U-Pb geochronology, fluid inclusion analysis and other geochemical analyses to elucidate high-resolution temporal fluid evolution in an old sedimentary basin with a complex tectonic history, providing a new paradigm for studying geofluid evolution.

### Hosted file

si-1.docx available at https://authorea.com/users/540489/articles/600237-direct-dating-paleo-fluid-flow-events-in-sedimentary-basins

### Hosted file

tables_yang et al..docx available at https://authorea.com/users/540489/articles/600237-direct-dating-paleo-fluid-flow-events-in-sedimentary-basins

### Hosted file

si-2.docx available at https://authorea.com/users/540489/articles/600237-direct-dating-paleo-fluid-flow-events-in-sedimentary-basins

# Direct dating Paleo-fluid flow events in sedimentary basins

P. Yang[1], K. Liu[1,2,*], Z. Li[3], K. Rankenburg[3], B. I. A. McInnes[3], J. Liu[1], N. J. Evans[3,4]

[1]Key Laboratory of Deep Oil and Gas, China University of Petroleum, Qingdao, China, [2]National Laboratory for Marine Science and Technology, Qingdao, China, [3]John de Laeter Centre, Faculty of Science and Engineering, Curtin University, Perth, Australia, [4]School of Earth and Planetary Sciences, Curtin University, Perth, Australia

* Correspondence to: K. Liu, liukeyu@upc.edu.cn

## Key Points

- Five fluid flow events from 353 Ma to 316 Ma are identified using *in-situ* U-Pb dating and fluid inclusion analysis in a calcite vein
- First oil charge in the Tabei Uplift of the Tarim Basin occurred around 325.8 Ma
- We propose a new paradigm for studying basin fluid evolution involving coupled *in situ* isotopic dating and fluid inclusion analysis

## Abstract

Reconstructing fluid evolution history in old sedimentary basins is extremely challenging due to the prolonged evolution, lack of exact age constraints and absence of preserved fluids. By integrating *in-situ* calcite U-Pb dating, fluid inclusion analysis, and high-resolution measurements of carbon-oxygen-strontium isotopes and rare earth elements (REEs), we have reconstructed the fluid evolution history in an Ordovician deeply-buried carbonate reservoir in the Tarim Basin, China with unprecedented temporal resolution. Five generations of calcite cementation spanning over 37 m.y. are dated in a single calcite vein with U-Pb ages ranging from ~353 Ma to ~316 Ma. The initial cement was associated with an intrusion of hyper-saline brine enriched REEs. This was followed by influx of meteoric water to precipitate the second and third generations of cement, characterized by a reduced salinity, anomalously high Sr isotopic ratios and extremely low concentrations of REEs. The fourth generation of cement was formed in a deep-fluid system accompanied by oil charge as indicated by the presence of bitumen, oil inclusions and lighter C and Sr isotope ratios. The fifth generation of cement was precipitated from an equilibrated connate water, having the lowest salinity and a comparable REE signature with the host rock. Oil charge was dated to be around 326 Ma. This study demonstrates the effectiveness in combining *in-situ* calcite U-Pb geochronology, fluid inclusion analysis and other geochemical analyses to elucidate high-resolution temporal fluid evolution in an old sedimentary basin with a complex tectonic history, providing a new paradigm for studying geofluid evolution.

## Plain Language Summary

In studying fluid evolution of old sedimentary basins, we are constraint by the lack of preserved fluids and precise timing of fluid events. We have, for the first time, coupled in-situ U-Pb dating of calcite cement and analysis of minute fluids trapped (fluid inclusions) within to investigate the fluid evolution of an old and deeply-buried carbonate reservoir in the Tarim Basin, western China with unprecedented temporal resolution. Five generations of calcite cementation with fluid inclusions in a single calcite vein of 2 cm across have been identified and dated, recording consecutive fluid flow events within 37 million years. It is found that the first cement was formed during an intrusion of hyper-saline brine at 353.0 Ma. The second (336.4 Ma) and third (336.3 Ma) generations were precipitated with an input of meteoric water. The fourth generation of cement was formed in association with oil charge at 325.8 Ma. The fifth generation of cement was precipitated from an equilibrated deep formation water at 315.5 Ma. Our study shows that by combining in-situ calcite U-Pb dating and fluid inclusion analysis, fluid evolution in old sedimentary basins can be effectively deciphered, offering a new paradigm for basin analysis.

***Keywords:*** Fluid flow; *In-situ* calcite U-Pb dating; Fluid inclusions, Isotope geochemistry, Carbonate reservoir; Tarim Basin

## 1. Introduction

Fluid flow in porous rocks is the most significant agent for material transportation in sedimentary basins (Seewald, 1994; Parnell, 1998; Bjørlykke and Jahren, 2012), exerting principal control on reservoir heterogeneities and hydrocarbon mobilization and accumulation (Liang et al., 2018; Pagel et al., 2018). Adequately reconstructing the chronology of fluid flow events in sedimentary basins is vital for understanding the basin evolutionary process and de-risking petroleum exploration. Recent advances in fluid flow event identification and characterization have been involved in utilizing the contact relationships between authigenic cements and host rock and the paragenesis of different cements for determining episodes of fluid circulation (Hyodo et al., 2014). It is common practice to combine fluid inclusion analysis with basin modeling to document fluid flow events (Karlsen et al., 1993; Parnell, 1998). However, previous workers (Braun and Burnham, 1992; Bodnar, 2003; Bourdet and Pironon, 2008; Yang and Liu, 2020) have suggested that poor preservation, re-equilibration and flawed measurement protocol of fluid inclusions can result in incorrect interpretation of the timing of fluid flow events when combined

59 with poorly constrained input parameters for basin modeling (e.g., paleo-tectonic configuration, paleo-
60 heat flow rates and amount of stratal hiatus), especially for old and deeply buried sedimentary basins
61 with complex tectonic and fluid evolution histories (Dyman et al., 1997; Zhu et al., 2019).

62 Various attempts have been made to direct date fluid flow events based on the radioactive isotope
63 principle, including $^{40}Ar/^{39}Ar$ dating of multi-generation overgrowths of K-feldspar (Mark et al., 2005).
64 However, this method has limited application in sedimentary basins, especially for carbonate sequences,
65 due to stringent sample requirements (Mark et al., 2008). *In-situ* laser-ablation U-Pb dating of carbonates
66 has recently become a research focus in the field of isotope geochronology (Li et al., 2014; Coogan et
67 al., 2016; Roberts and Walker, 2016; Roberts et al., 2020). Compared with the conventional isotope
68 dilution method, it bears the advantages of simple sample preparation, high spatial resolution and high
69 measurement efficiency, and shows the potential of accurate dating of multi-generation carbonate
70 cements (Godeau et al., 2018). The technique has successfully been used to determine the age of
71 carbonate minerals in oceanic crust (Coogan et al., 2016), delineate fault activity events (Roberts and
72 Walker, 2016; Nuriel et al., 2017) and characterize the diagenetic history of carbonate reservoirs (Godeau
73 et al., 2018). By integrating *in-situ* laser-ablation U-Pb dating of carbonate cements with fluid inclusion
74 and other geochemical analyses, here we attempt to constrain the fluid flow events in old and deeply
75 buried sedimentary basins where reconstruction of burial and thermal histories is extremely complex.

76 The Tabei Uplift, located in the northern Tarim Basin, is one of the deepest and most important
77 petroleum producing areas in China, with over 3 billion tons of oil-equivalent discovered in the Paleozoic
78 carbonates (Pang et al., 2010). The main oil-producing layers are the deeply buried Ordovician Yijianfang
79 ($O_2yj$) and Yingshan ($O_{1-2}y$) formations (> 4500 m). Despite numerous attempts made by previous
80 workers (e.g., Zhang and Luo, 2011; Zhu et al., 2013; Liu et al., 2017; Zhang et al., 2018; Han et al.,

2019; Ge et al., 2020), the exact timing of fluid flow events is still not well defined, due mainly to the poorly constrained burial and thermal histories of the basin (Li et al., 2010; Wang et al., 2010; Qiu et al., 2012; Xu et al., 2018; Liu et al., 2020). In this contribution, the fluid flow events are elucidated from a calcite vein with unprecedented temporal resolution in a deep carbonate reservoir (> 5800 m) by combining *in-situ* calcite U-Pb dating with fluid inclusion, carbon-oxygen-strontium isotopes, and major and minor element analyses. The main objectives are to: (1) delineate the absolute timing of different fluid flow events; (2) determine origins of different diagenetic fluids; and (3) establish the fluid evolution model during the Carboniferous in the deep carbonate reservoir. The results are beneficial to shed light on the fluid evolution history of the Tarim Basin and similar old and deeply buried sedimentary basins around the world, providing a new paradigm for studying geofluid evolution.

## 2. Geological Setting

The Tarim Basin, covering an area of approximately $560 \times 10^3$ km$^2$ (Figure 1a), is the largest inland petroliferous basin in China (Li et al., 1996; Jia and Wei, 2002). It is a giant superimposed basin, composed mainly of Paleozoic marine cratonic basin sequences and Meso-Cenozoic continental foreland basin sequences overlying a continental crustal basement (Jia and Wei, 2002). The basin has experienced seven tectonic evolution stages (Li et al., 1996), and comprises ten first-order tectonic units. The sedimentary strata of the basin are characterized by Cambrian-Ordovician shallow marine-lagoonal carbonate rocks, Silurian-Devonian marine clastic rocks, Carboniferous-Permian marine-terrestrial transitional sandstones and mudstones, and Mesozoic-Cenozoic terrestrial sedimentary rocks (Zhang and Huang, 2005).

The Tabei Uplift in the Tarim Basin, western China (Fig. 1) is an east-west trending tectonic unit with

positive topographic relief in the northern part of the basin and has gone through multi-phase tectonic movements along with frequent fault activities and fluid flow events (Li et al., 1996; Jia and Wei, 2002). During the Early Devonian, intense tectonic uplift and exhumation resulted in extensive development of faults and massive denudation of up to 3000 m of the Silurian and Upper Ordovician strata in the area (Lin et al., 2012). Exposed carbonate rocks of the Lower-Middle Ordovician Yingshan ($O_{1\text{-}2}y$) and Yijianfang ($O_2yj$) formations were subject to karstification with the formation of fractures, cave networks, vugs and solution-dominated landforms (Liu et al., 2017). During the Late Devonian to Early Carboniferous, marine water inundated the Tabei area, leading to successive deposition of glutenite of braided river delta facies, lagoonal mudstone, and limestone and salt of saline lagoon facies of the Tournaisian Bachu Formation ($C_1b$) (Fig. 1; Wu et al., 2008). The Tabei Uplift experienced an overall subsidence in the Carboniferous. The late Hercynian (Late Permian) tectonic movement also promoted intensive tectonic uplift and exhumation of the Tabei Uplift along with magmatic activity events (Zhu et al., 2013), causing the loss of the entire Permian and most of the Carboniferous sequences. Since the Indosinan orogeny (Triassic), the Tabei Uplift has experienced continued subsidence. The present tectonic configuration came to being during the Himalayan orogeny (Paleogene-Neogene). The TK721 well investigated in this paper is located in the southern paleo-slope of the Tabei Uplift (Figure 1a), where the Bachu Formation is composed mainly of lagoonal mudstone, limestone and salt of saline lagoon facies (Figure 1b).

## 3. Material and Methods

A core sample containing calcite veins that occur at a high-angle to the stratal surface (supplementary Figure S1) was obtained from the $O_{1\text{-}2}y$ oil-bearing carbonate reservoir in Well TK721 in the Tabei Uplift at a depth of 5842.60–5842.75 m (Figure 1b). The sample was characterized petrographically using

optical microscopy (Zeiss Axio Imager A2m) and imaged by Cathodoluminescence (CL) using a Relion III cold-cathode device at beam voltages of up to 15 keV and an electric current of 500 μA. Selected thin sections were examined under a Zeiss Crossbeam 550 FIB-SEM integrated with a Bruker EDX analysis system (XFlasher Detector 430-M).

Doubly polished wafers of approximately 80 μm in thickness were prepared for fluid inclusion petrography and microthermometry analysis. Microscopic observation of fluid inclusions was carried out using a Zeiss Axio Imager A2m microscope equipped with transmitted and fluorescent light capabilities. Micro-fluorescence spectra of oil inclusions were obtained using a Horiba iHR320 imaging spectrometer coupled to a Zeiss Axio Imager A2m microscope with a 100 W high pressure mercury-vapor light source. $\lambda_{max}$ (wavelength of the maximum intensity in the fluorescence spectrum) was obtained to characterize the gross composition of the inclusion oil. Microthermometry measurements of fluid inclusions were conducted with a Linkam THMSG600 heating-freezing stage using the cycling technique proposed by Goldstein and Reynolds (1994). The measurement precision was ± 1 ℃ for the homogenization temperature (Th) and ± 0.1 ℃ for the final ice melting temperature (Tm), respectively. The heating-freezing stage was calibrated using synthetic $CO_2$-$H_2O$ inclusions (Tm = -56.6 ℃) and pure $H_2O$ aqueous inclusions (Tm = 0 ℃) at low temperature. The NaCl-equivalent salinity of aqueous inclusions was calculated based on the equation proposed by Bodnar (1993). Considering the potential effect of fluid inclusion re-equilibration in calcite (Goldstein and Reynolds, 1994; Bodnar, 2003), the minimum Th value of aqueous inclusions in each generation of calcite cement was used to represent the minimum trapping temperature.

Calcite veins and the surrounding host rock fragment were physically separated from the polished carbonate chips using a micro mill fitted with a 100-micron bit under transmitted light, and were selected

for carbon and oxygen isotope analysis. The calcite samples were reacted with 100% phosphoric acid for 4 hours at 25 ℃. The carbon and oxygen stable isotope analysis was conducted using a Finnigan Delta S mass spectrometer. Oxygen and carbon isotope data are presented relative to Pee Dee Belemnite (VPDB) in the conventional $\delta^{13}C$ and $\delta^{18}O$ notations respectively. Replicated analyses are reproducible to ±0.1‰ for both $\delta^{13}C$ and $\delta^{18}O$.

Major element abundances of the calcite vein and carbonate rock were analyzed by wavelength-dispersive spectrometry (WDS) on a JEOL JXA-8230 electron probe, with an accelerating voltage of 15 kV and a beam current of 20 nA and a beam diameter of 5–8 μm. Natural minerals and synthetic oxides were used as standards. The analytical uncertainty is 1.5% or less. Trace element concentrations in calcite vein and carbonate rock were measured on thin sections by LA-ICP-MS at the State Key Laboratory of Ore Deposit Geochemistry, Institute of Geochemistry, Chinese Academy of Sciences, using an Agilent 7700 × ICP-MS equipped with a GeoLasPro 193 nm ArF-excimer laser. Analyzed conditions are shown in Tang et al. (2020). A laser repetition of 6 Hz, energy density of 5.0 J $cm^{-2}$ and spot size of 60 μm was used for this analysis. The ablation time for each sample point was 60 seconds. NIST SRM 610 glass was used to optimize mass responses and minimize oxide levels. NIST612 was used for external calibration and drift correction and USGS MACS-3 carbonate standard was used to detect the consistency and reproducibility of the sample data. $^{43}Ca$ was used as an internal standard. Data reduction was processed using the ICPMSDataCal software. The average CaO contents for the same phase of calcite obtained by electron microprobe analysis were used for internal calibration.

*In-situ* calcite Sr isotope measurements were conducted on a Nu Plasma III MC-ICP-MS (Nu Instruments) coupled to a RESOlution-S155 ArF193-nm laser ablation system (Australian Scientific Instruments) at the State Key Laboratory of Ore Deposit Geochemistry, Institute of Geochemistry,

Chinese Academy of Sciences. Calcite was spot ablated in a mixture of He (350 ml $min^{-1}$) and $N_2$ (2 ml $min^{-1}$) gas using the following parameters: 30 s baseline acquisition, 40 s ablation, 228 μm beam diameter, 10 Hz repetition rate and 5 J $cm^{-2}$ energy density. The analytical and interference correction protocols follow those described in Ramos et al. (2004) as fully addressed in Gao and Zhou (2013). An in-house standard consisting of a modern-day coral was ablated once every five samples. In this study, repeated analyses of a modern-day coral yielded an average $^{87}Sr/^{86}Sr$ ratio of 0.70920 ± 0.00003 (n = 7), comparable with the value (0.70923 ± 0.00002) obtained using TIMS (Chen et al., 2018).

Laser ablation inductively coupled plasma mass spectrometry (LA-ICP-MS) was performed at the GeoHistory Facility in the John de Laeter Centre, Curtin University, Perth, Australia, on polished thin sections after initial identification of high-purity calcite grains via Tescan Integrated Mineral Analyzer (TIMA). Ablations utilized an ASI RESOlution-SE 193 nm excimer laser controlled by GeoStar μGIS™ software. Laser fluence was calibrated above the sample cell using a hand-held energy meter, and subsequent analyses were performed in constant energy mode. The Laurin Technic S155 sample cell was flushed with ultrahigh purity He (320 mL $min^{-1}$) and $N_2$ (1.2 mL $min^{-1}$), both of which were passed through separate inline Hg traps. High-purity Ar was used as the ICP-MS carrier gas (flow rate ~1 L $min^{-1}$). Elemental abundances were measured using an Agilent 8900 QQQ quadrupole ICP-MS operated in single quad mode. Each analytical session consisted of initial gas flow and ICP-MS ion lens tuning for sensitivity and robust plasma conditions ($^{238}U/^{232}Th$ ~1; $^{206}Pb/^{238}U$ ~ 0.2; and $^{238}UO/^{238}U$ < 0.004). Pulse-analog (P/A) conversion factors were determined on the NIST 610 reference glass by varying laser spot sizes and/or laser repetition rate to yield 1–2 Mcps per element. Laser ablation parameters were 87 μm spot diameter, 10 Hz repetition rate, and on-sample laser energy of 4 J $cm^{-2}$. After two initial cleaning pulses, $^{25}Mg$, $^{46}Ca$, $^{55}Mn$, $^{206}Pb$, $^{207}Pb$, $^{208}Pb$, $^{232}Th$, and $^{238}U$ were collected with dwell times of 5, 5, 5,

20, 20, 10, 10, and 20 ms, respectively, for 60 s ablation periods after 40 s of baseline acquisition. The time-resolved mass spectra were reduced using the 'UPb_CommonApproach' data reduction scheme in Iolite 3.7 (Paton et al., 2011 and references therein). The primary reference material used in this study for the determination of $^{238}U/^{206}Pb$ and $^{207}Pb/^{206}Pb$ fractionation factors was natural calcite spar WC-1 (254.4 ± 6.4 Ma, Figure S2; Roberts et al., 2017) interspersed with the unknown samples in a ratio of about 1:10. Discordia ages were then calculated for WC-1 and all samples using IsoplotR (Vermeesch, 2018). Interpretation of U-Pb age presentation is presented in the supplementary materials.

# 4. Results

## 4.1. Calcite vein petrography

Five generations of calcite cement (sequentially named C1, C2, C3, C4 and C5) based on paragenetic relationships can be identified in the carbonate vein (Figure 2a and b). C1 displays dark orange luminescence and is characterized by a bladed crystal morphology with long axis perpendicular to the host rock. C2 crystallized on the C1 substrate, but is separated by a "dust rim", consisting mainly of detrital quartz grains (Figure 2c). C2 contains mostly rhombic calcite crystals with orange luminescence, while C3 features euhedral to subhedral calcite crystals displaying dark orange luminescence with weak crystal zonation. Some anhedral C3 calcite cement fills the residual space between euhedral or subhedral C3 calcite crystals (Figure 2a). C4 occurs mainly between C1 and C5, and is characterized by blocky or mosaic aggregates with bright orange luminescence. Minor C4 calcite is also present in the dissolution pores within C3 and as fracture fillings within C1 (Figure 2b). Bitumen is a significant new phase present in the dissolution pores within C3 (Figure 2d) and between the C1 and C4 calcite cements (Figure 2e). C5 occurs between the C4 calcite cement and the host rock, and is composed of blocky or mosaic

aggregates displaying orange luminescence with minor dark orange patches. Some bitumen also occurs along the boundary of the C4 and C5 calcite cements.

### 4.2. Fluid inclusion analysis

Fluid inclusion assemblages (FIAs, Goldstein and Reynolds, 1994) of primary aqueous inclusions occur in all five generations of calcite cement, with typical dimensions of 5–20 μm. The FIAs are present either in groups or as isolated occurrences. The majority of the FIAs are diphasic (liquid-vapor) inclusions at room temperature, with vapor filling degrees commonly less than 5%. Some aqueous inclusions in C1 are monophasic (liquid only). The microthermometric data of primary aqueous inclusions are shown in the supplementary Table S1. Homogenization temperatures (Th) of the diphasic aqueous inclusions from C1 to C5 are in the range of 46.5–118.6 °C, 50.8–112.5 °C, 58.5–106.5 °C, 86.5–114.6 °C and 103.7–161.3 °C, respectively (Figure 3a), with corresponding final ice melting temperatures (Tm) being -20.8–-16.4 °C, -14.6–-10.8 °C, -12.8–-8.3 °C, -6.5–-4.8 °C and -4.2–-3.1 °C. The calculated NaCl-equivalent salinities are 19.8–22.9 wt.%, 14.8 – 18.3 wt.%, 12.0–16.7 wt.%, 7.6–9.9 wt.% and 5.1–6.7 wt.%, respectively (Figure 3a).

Oil inclusion assemblages (OIAs, Bourdet et al., 2012) mainly occur within C3, C4 and C5. In C3, OIAs occur mainly along annealed microfractures cutting cross dissolved calcite fabrics with bitumen (Figure 2f), indicative of a secondary origin (Goldstein and Reynolds, 1994). In C4 and C5, OIAs are commonly present in groups or as isolated occurrences immediately adjacent to the bitumen, with long axes of individual elongate inclusions parallel to the bitumen rims (Figure 2g and h), suggesting that these oil inclusions are of primary origin (Goldstein and Reynolds, 1994). Oil inclusions are primarily elliptic, elongated, square or irregular in shape, 5 – 15 μm in diameter with vapor bubbles occupying 5 –

10% in volume. The microthermometric data of oil inclusions are shown in the supplementary Table S2. These oil inclusions are characterized by orange-red florescence with fluorescence spectral peaks ($\lambda_{max}$) around 655 nm and Th values ranging from 64.1 °C and 76.5 °C with a mode of 65–70 °C (Figure 3b).

### 4.3. Major and Trace Elements

#### 4.3.1. Major Elements

Major element compositions for the calcite cements and carbonate host rock are shown in Table 1. The contents of CaO and MgO for the C1 calcite cement are in the range of 55.34–55.99 wt.% and 0.09–0.17 wt.%, respectively, with Mg/Ca ratios between 0.002 and 0.004. The CaO contents for the C2 and C3 calcite cements are 55.11–56.12 wt.% and 55.59–56.56 wt.%, respectively with corresponding MgO contents being 0.06–0.42 wt.% and 0.22–0.36 wt.%, and corresponding Mg/Ca ratios being 0.002–0.011 and 0.005–0.009. The CaO contents for the C4 calcite cement range from 55.42 wt.% to 57.12 wt.%, and the MgO contents are in the range of 0.06–0.10 wt.%, with Mg/Ca ratios between 0.002 and 0.003. The CaO and MgO contents for the C5 calcite cement vary from 55.17 wt.% to 56.93 wt.% and from 0.04 wt.% to 0.14 wt.%, respectively, with Mg/Ca ratios less than 0.003. The carbonate host rock has CaO contents of 55.46–56.62 wt.% and MgO contents of 0.03–0.32 wt.%. Their Mg/Ca ratios are from 0.001 to 0.008. The Mg/Ca ratios for the calcite cements and host rock are both less than 0.1, indicating that the vein and host rock are typical of low-Mg calcite. Other constituents in the calcite vein and host rock are quite low, commonly less than 0.10 wt.% (Table 1).

#### 4.3.2. Trace Elements

Trace element abundances in the C1-C5 calcite cements and carbonate host rock are presented in the supplementary Table S3. REE + Y concentrations were normalized to the Post-Archen Australian Shale

253 (PAAS; Mclennan, 2001). The ratios related to REE + Y concentrations calculated by the PAAS
254 normalization is presented in Table 2 and Figure 4 to manifest the geochemical characteristics for the
255 C1-C5 calcite cements and host rock.

256 (1) The REE concentrations for the C1 calcite cement vary from 4.92 ppm to 16.67 ppm and
257 the REE + Y patterns are characterized by uniform HREE depletion with [Pr/Yb] in the
258 range of 1.25–4.95, [Pr/Tb] of 0.58–1.49 and [Tb/Yb] of 1.84–4.15 (Figure 4a), positive La
259 anomalies with [La/La*] in the range of 1.72–2.51, negative Ce anomalies with [Ce/Ce*] in
260 the range of 0.74–0.83, positive Gd anomalies with [Gd/Gd*] higher than 1.0 except for one
261 sampling spot (0.86), no obvious Er anomalies with [Er/Er*] in the range of 0.61–1.12,
262 minor positive Eu anomalies with [Eu/Eu*] slightly higher than 1.0, except for one sampling
263 spot (0.97).

264 (2) The REE concentrations for the C2 calcite cement are in the range of 0.20 ppm to 0.41 ppm
265 and the REE + Y patterns are characterized by uniform LREE depletion with [Pr/Yb] in the
266 range of 0.18–0.47, [Pr/Tb] of 0.25–0.44 and [Tb/Yb] of 0.68–1.06 (Figure 4b), positive La
267 anomalies with [La/La*] of 1.58–2.05, except one sampling spot (0.28), negative Ce
268 anomalies with [Ce/Ce*] in the range of 0.74–0.94; slight positive Gd anomalies with
269 [Gd/Gd*] in the range of 1.01–1.24, no obvious Er anomalies with [Er/Er*] in the range of
270 0.83–1.54; negative Eu anomalies with [Eu/Eu*] in the range of 0.31–0.53. The REE
271 concentrations for the C3 calcite cement is extremely low, less than 0.10 ppm with the
272 contents of some REEs even below the detection limit.

273 (3) The REE concentrations for the C4 calcite cement range from 1.05 ppm to 4.47 ppm and

the REE + Y patterns are characterized by minor HREE depletion with [Pr/Yb] in the range of 1.34–2.50, [Pr/Tb] of 0.64–1.30 and [Tb/Yb] of 2.11–3.11 (Figure 4c); positive La anomalies with [La/La*] in the range of 1.13–1.64, minor negative Ce anomalies with [Ce/Ce*] in the range of 0.92–0.95, no obvious Gd, Er and Eu anomalies with [Gd/Gd*] in the range of 0.46–1.78, [Er/Er*] of 0.67–1.03 and [Eu/Eu*] of 0.43–1.15.

(4) The REE concentrations for the C5 calcite cement vary from 2.33 ppm to 8.40 ppm and the REE + Y patterns are characterized by relatively unfractionated REE + Y patterns with [Pr/Yb] in the range of 0.85–1.16, [Pr/Tb] of 0.74–1.09 and [Tb/Yb] of 0.89–1.47 (Figure 4d), no obvious La and Ce anomalies with [La/La*] in the range of 0.72–1.73 and [Ce/Ce*] close to 1.0, positive Gd anomalies with [Gd/Gd*] in the range of 1.06–1.80, except for two sampling spots (0.97 and 0.98), no obvious Er anomalies with [Er/Er*] in the range of 0.75–1.18, positive Eu anomalies with [Eu/Eu*] in the range of 1.06–1.39, except for one sampling spot (0.92).

(5) The REE concentrations for the host rock range from 2.63 ppm to 2.99 ppm and the REE + Y patterns are characterized by uniformly unfractionated REE + Y patterns with [Pr/Yb] in the range of 0.85–1.16, [Pr/Tb] of 0.74–1.09 and [Tb/Yb] of 0.89–1.47 (Figure 4e), no obvious La and Ce anomalies with [La/La*] in the range of 0.42–1.70 and [Ce/Ce*] close to 1.0, no obvious Gd, Er and Eu anomalies with [Gd/Gd*] in the range of 0.69–1.44, [Er/Er*] of 0.79–1.21 and [Eu/Eu*] of 0.60–1.17.

In summary, C1 is enriched with REEs, while C2 and C3 contains the lowest REEs, which are an order of magnitude less than that in C1. The REE + Y characteristics for the C4 calcite cement are similar to

295 that for the C1 calcite cement, while the REE + Y characteristics for the C5 calcite cement are almost the
296 same as that for the host rock (Figure 4f).

297 **4.4. Carbon, Oxygen and Strontium Isotopes**

298 Carbon, oxygen and strontium isotope ratios for the C1-C5 calcite cements and carbonate host rock
299 are presented in Table 3 and Figure 5. The $\delta^{13}C_{V\text{-}PDB}$ values for the C1 to C5 calcite cements are -5.4‰,
300 -8.6‰, -9.9‰, -9.0‰ and -4.3‰, respectively, and the corresponding $\delta^{18}O_{V\text{-}PDB}$ values are -3.2‰, -
301 11.4‰, -12.7‰, -13.8‰ and -13.6‰. The $\delta^{13}C_{V\text{-}PDB}$ and $\delta^{18}O_{V\text{-}PDB}$ values for the carbonate host rock are
302 -2.2‰ and -7.6‰, respectively. The strontium (Sr) isotope ratios for the C1-C5 cements and host rock
303 are shown in the Table S4 and Figure 5. The $^{87}Sr/^{86}Sr$ values for the C1 to C5 calcite cements are in the
304 range of 0.70816–0.70855, 0.71024–0.71034, 0.71036–0.71046, 0.70913–0.70926, 0.70898–0.70929,
305 respectively. The $^{87}Sr/^{86}Sr$ ratios for the host rock range from 0.70874 to 0.70888.

306 **4.5. *In-situ* Calcite U-Pb Dating**

307 The C1 calcite cement yields a Tera-Wasserburg lower intercept age of 353.01 ± 2.66 Ma (1σ; Figure
308 6a; the uncertainty of the age of the WC1 standard is not propagated). The lower intercept ages obtained
309 from C2 and C3 calcite cements are equivalent within uncertainty, namely, 336.42 ±1.60 Ma and 336.34
310 ± 3.33 Ma (Figure 6b and c). C4 yields a lower intercept age of 325.82 ± 3.74 Ma (Figure 6d) and the
311 lower intercept age of C5 is 315.52 ± 3.22 Ma (Figure 6e). The lower intercept age for the surrounding
312 carbonate host rock is 470.80 ± 2.27 Ma (Figure 6f).

# 5. Discussion

## 5.1. Origin of Diagenetic Fluids

In the calcite vein analyzed, C1 is the oldest, followed by C2, C3, C4 and C5 sequentially (Figure 6). The U-Pb ages obtained from the five generations of cement range from 353 Ma to 316 Ma, covering almost the entire Carboniferous period (358.9–298.9 Ma). The lower intercept age for the host rock is 470.80 ±2.27 Ma (Figure 6a) within the biostratigraphic age range of the Yingshan Formation (Fu, 2019). The $\delta^{13}C_{V\text{-}PDB}$ and $\delta^{18}O_{V\text{-}PDB}$ values for the carbonate host rock (Figure 5) are similar with that for the Ordovician carbonate rocks in the Tabei area obtained previously (Liu et al., 2017; Han et al., 2019), and the $^{87}Sr/^{86}Sr$ ratios for the host rock are consistent with that of the contemporaneous sea water during the Ordovician period (McArthur et al., 2001). The uniformly unfractionated REE + Y patterns for the carbonate host rock (Figure 4e) are different from the typical REE + Y patterns for marine carbonates (Webb and Kamber, 2000; Shields and Webb, 2004), implying that the primary REE + Y characteristics for the carbonate host rock have been altered by diagenesis (Van Kranendonk et al., 2003; Nothdurft et al., 2004). Compared with the host rock, the calcite cements are characterized by low contents of $SiO_2$ and $Al_2O_3$, Ti, Th and U (Tables 1 and S3), indicating that the REE + Y patterns for the calcite cements had not been or only slightly affected by diagenetic alterations (Kamber and Webb, 2001; Zhao and Zheng, 2013), and thus can represent the geochemical signature of the primary calcite cements.

From C1 to C5, the minimum Th value of primary aqueous inclusions for each generation of calcite cement increases progressively, whereas the corresponding salinity value decreases successively (Figure 3a). The bladed crystal morphology of the C1 calcite cement is typical of calcite formed in the marine phreatic zone (Moore and Wade, 2013) and the presence of monophasic inclusions in C1 also indicates

that the cement was formed in a near-surface diagenetic environment (Goldstein and Reynolds, 1994). U-Pb dating results (Figure 6a) indicate that the C1 calcite cement was precipitated in the Tournaisian. The $^{87}Sr/^{86}Sr$ ratio for the C1 calcite cement is lower than that of the Ordovician carbonate host rock (Figure 5), but similar to that of sea water during the Tournaisian (McArthur et al., 2001), indicating that the C1 cement was precipitated from fluids related to the contemporaneous sea water. C1 is also comparatively enriched with REEs compared with the host rock and other generations of cement in the calcite vein (Table 2). During the Tournaisian, the Tabei Uplift was characterized by a hyper-saline lagoonal environment (Wu et al., 2008), which may provide material source for C1 precipitation via faults and fractures, explaining the occurrence of primary high-salinity aqueous inclusions (19.8–22.9 wt.% $NaCl_{eq}$) and enriched REEs in the C1 calcite cement (Frimmel, 2009), and a relatively high $\delta^{18}O_{V-PDB}$ value (Robinson and Gunatilaka, 1991). The increase of $^{87}Sr/^{86}Sr$ values for the C2 and C3 calcite cements (Figure 5) relative to that for C1 and the carbonate host rock may suggest an intrusion of meteoric water into the calcite vein system (Palmer and Elderfield, 1985; Palmer and Edmond, 1989), as evidenced from an overall decrease of $\delta^{13}C_{V-PDB}$ and $\delta^{18}O_{V-PDB}$ values (Allan and Matthews, 1982; Lohmann, 1988; Hays and Grossman, 1991) and inclusion salinities (Figure 3a), and extremely low concentrations of REEs in C2 and C3 (Table 2). Taking the minimum Th (50.8 °C and 58.5 °C) of primary aqueous inclusions and $\delta^{18}O_{V-PDB}$ values (-11.4‰ and -12.7‰) for the C2 and C3 calcite cements into consideration, the calculated $\delta^{18}O$ values for the C2 and C3 calcite cements are -4.7‰ and -4.8‰ relative to SMOW (Friedman and O'Neil, 1977), respectively, similar to the isotope compositions ($\delta^{18}O_{SMOW}$ = -4.0‰) of the mean worldwide meteoric water (Craig and Gorden, 1965), indicative of involvement of meteoric water during the precipitation of C2 and C3 calcite cements. The associated "dust rim" on the substrate of C2 and C3 calcite cements (Figure 2a) indicates the influx of meteoric

356 water was accompanied by infiltration of fine detrital sediments from the overlying strata. The extremely
357 low concentrations of REEs for the C2 and C3 calcite cements (Table 2) are also supportive of
358 involvement of meteoric water in the diagenetic alterations (Bolhar and Van Kranendonk, 2007).

359 The $\delta^{13}C_{V\text{-}PDB}$ value for the C4 calcite cement is similar to that for C2 and C3, whereas their
360 corresponding REE + Y patterns and $^{87}Sr/^{86}Sr$ ratios are quite different (Figs. 4 and 5), suggesting that
361 there is little or no influence of meteoric water on the C4 calcite precipitation. The similarity of Sr
362 isotopic ratios for the C4 calcite cement and the host rock (Figure 5) indicates a predominant contribution
363 of marine carbonate connate water during the formation of the C4 calcite cement. The presence of
364 bitumen rim between the C1 and C4 calcite cements and oil inclusions of primary origin in the C4 calcite
365 cement (Figure 2g and h) indicates the occurrence of oil emplacement during the C4 calcite precipitation,
366 as well as the presence of C4 crystals in the dissolution pores within the C3 calcite cement (Figure 2a).
367 The low $\delta^{13}C_{V\text{-}PDB}$ value for the C4 calcite cement may reflect light carbon ($^{12}C$) contributed from the
368 charged oil, while the low $\delta^{18}O_{V\text{-}PDB}$ value may be attributed to temperature change (Schmidt et al., 2005)
369 during C4 cementation as evidenced by an increased Th values of primary aqueous inclusions in the C4
370 cement (Figure 3a).

371 Compared with C4, the $\delta^{13}C_{V\text{-}PDB}$, $^{87}Sr/^{86}Sr$ and REE ratios for the C5 cement resemble more to that
372 of the host rock (Figs. 4F and 5), indicating that C5 was formed predominantly by the connate water
373 within the host rock. The occurrence of bitumen and oil inclusions of primary origin in the C5 calcite
374 cement demonstrates the presence of oil during C5 precipitation. The NaCl-equivalent salinities of
375 primary aqueous inclusions in the C4 and C5 calcite cement decrease from 7.6–9.9 wt.% to 5.1–6.7 wt.%
376 (Figure 3a), possibly reflecting that the reservoir formation water was progressively equilibrated with the
377 connate water in the Ordovician host rocks.

## 5.2. Timing of Oil Charge Event

The absence of bitumen and primary oil inclusions in the C1 and C2 calcite cements indicate that the formation of the C1 and C2 calcite cements predated the oil charge. The extensive dissolution of the C3 calcite cement and the presence of bitumen and secondary oil inclusions in the C3 calcite cement suggest that the oil charge post-dated the C3 calcite precipitation. In comparison, the presence of bitumen rim between the C1 and C4 calcite cements and oil inclusions of primary origin in C4 indicates the emplacement of oil was contemporaneous with the C4 calcite precipitation. The consistency of the oil inclusions in C3 and C4 calcite cements in terms of fluorescence colors, spectral parameters, and homogenization temperatures (Th) (Figure 3b) suggests that they were formed during the same oil charge event. Some euhedral C4 calcite crystals are present in the dissolution pores within the C3 calcite cement, further verifying that the concomitant oil charge and the C4 calcite precipitation. In summary, the earliest oil charge event occurred during the C4 calcite precipitation, around 325.82 ± 3.74 Ma.

Tremendous efforts have been made to date the oil charge history in the Tabei Ordovician carbonate reservoirs (Zhang and Luo, 2011; Zhu et al., 2013; Zhang et al., 2018; Ge et al., 2020). For example, using K-Ar dating of authigenic illites, Zhang and Luo (2011) insisted that the overlying Silurian oil pools were mainly formed during the Early Permian (277 Ma to 293 Ma). Based on Th data of aqueous inclusions and 1D basin modelling, Zhu et al. (2013) and Ge et al. (2020) concluded that oil migration and accumulation occurred during the Middle Permian-Early Triassic around 280–230 Ma. In comparison, the oil charge timing (*ca*. 326 Ma) obtained in the present study is much earlier than previously thought, and this new oil charge timing may arouse people to reconsider the oil charge history and modulate exploration strategy in the Tabei area.

### 5.3. Fluid Evolution Reconstruction

Our interpretation of the cementation process in the calcite vein can be summarized as follows (Figs. 7 and 8): In the Tournaisian, the Tabei area was dominated by a hyper-saline lagoon environment (Wu et al., 2008). Possibly triggered by regional tectonic movement, the initial opening of some high-angle faults promoted the downward influx of hyper-saline brine in the lagoon into the immediately underlying Ordovician carbonate rocks via extensively developed fractures, cavens and vugs (Figure 8a), and resulted in the precipitation of C1 at 353 Ma (Figure 7). C1 thus contains some hyper-saline brine inclusions and enriched with REEs. In the Visean (*ca.* 336 Ma), possibly caused by sea-level falls (Haq and Schutter, 2008) or regional tectonic activities, the Tabei area was partially exposed and affected by meteoric water via faults and regional unconformities from the elevated watershed to the north (Figure 8b). The intrusion of meteoric water lowered the salinity and the concentrations of REEs of the formation water in the fault-fracture system, and caused the precipitation of C2 and C3 cements in the calcite vein (Figure 7). The influx of meteoric water was accompanied by infiltration of fine detrital sediments from the overlying strata, forming “dust rim” on the substrates of the C2 and C3 calcite cements (Figure 2a). Attributed to the involvement of meteoric water, the salinities of aqueous inclusions in the C2 and C3 calcite cements decreased from 14.8–18.3 wt.% to 12.0–16.7 wt.%, and the concentrations of REEs were reduced to baseline values or below detection limit. In the Serpukhovian (~326 Ma), the Ordovician carbonate rock was buried sufficiently deep, preventing any penetration by surface water (meteoric or sea water; Figure 8c). Reactivation of faults was accompanied by oil charge from the source rocks below. $CO_2$ and organic acids associated with oil charge led to dissolution of the host rock and the early calcite cements, forming secondary oil inclusions along annealed microfractures in the C3 calcite cement. The carbon sources for the C4 calcite cementation were thus composed of both organic carbon and marine

carbonate. Bitumen rim is present along the boundary between C1 and C4 and oil inclusions of primary origin are present in the C4 calcite cement. At the end of the Bashkirian (~316 Ma), the last fracture-opening event occurred in the calcite vein system, forming the C5 calcite cement (Figure 8d). The formation water in the vein would be in equilibrium with the connate water within the host rock because the carbon and strontium isotope ratios and REE signatures for the C5 calcite cement are comparable to that of the host rock, and the salinity of brine inclusion in the vein system is consistent with the connate water salinity.

## 6. Conclusions

By combining in-situ calcite U-Pb geochronology, fluid inclusion analysis and other geochemical measurements, this study elucidates high-resolution temporal fluid evolution in a Paleozoic sedimentary basin with a complex tectonic history. This innovative workflow provides an alternative to the conventional coupled fluid inclusion-basin modeling approach in studying geofluid evolution in sedimentary basins.

Through a successful characterization of fluid evolution history spanning over 37 m.y. in a single 2 cm calcite vein, this study reconstructed the Carboniferous fluid evolution history in an Ordovician giant carbonate reservoir in the Tarim Basin, China. The bituminous calcite vein in the Ordovician carbonate reservoir records at least five generations of calcite precipitation from basinal fluids that compositionally evolved from ~353 to ~316 Ma. Fluid inclusion evidence indicates that fluid evolution is a response to progressive burial and frequent external fluid intrusions from ~353 to ~336 Ma, and the reservoir experienced oil charge at ~326 Ma, which continued until mineralization sealed the vein to fluid movement at ~316 Ma. This new oil charge timing is much earlier than previously thought (ca. 250 Ma)

based on conventional fluid inclusion homogenization temperature and basin modeling results, and may arouse people to reconsider the oil charge history and modulate exploration strategy in the study area, such as exploring for paleo-stratigraphic or structural traps that may have existed at ~326 Ma.

## Acknowledgments

This study was supported by the Chinese National Key R & D Project (2019YFC0605500), the Strategic Priority Research Program of the Chinese Academy of Sciences (XDA14010401), the National Natural Science Foundation of China (41821002), AuScope and the Australian Government via the National Collaborative Research Infrastructure Strategy, and the Australian Research Council LIEF program (LE150100013). We are grateful to Zhijun Jin of Peking University who introduced us to the research area and Huili Li of SINOPEC facilitating in the sampling. Our calcite U-Pb data associated with this article are available from Dataset S1 in the supporting information.

## References

Allan, J. R., & Matthews, R. K. (1982). Isotope signatures associated with early meteoric diagenesis. *Sedimentology*, *29*, 797–817. https://doi.org/10.1111/j.1365-3091.1982.tb00085.x

Bjørlykke, K., & Jahren, J. (2012). Open or closed geochemical systems during diagenesis in sedimentary basins: constraints on mass transfer during diagenesis and the prediction of porosity in sandstone and carbonate reservoirs. *AAPG Bulletin*, *96*, 2193–2214. https://doi.org/10.1306/04301211139

Bodnar, R. J. (1993). Revised equation and table for determining the freezing point depression of H2O-NaCl solutions. *Geochimica et Cosmochimica Acta*, *57*, 683–684. https://doi.org/10.1016/0016-7037(93)90378-A

462 Bodnar, R. J. (2003). Reequilibration of fluid inclusions. In: Samson, I., Anderson, A., Marshall, D. (Eds.),
463 Fluid inclusions: Analysis and interpretation. Mineralogy Association of Canada Short Course 32, pp.
464 213–230.

465 Bolhar, R., & Van Kranendonk, M. J. (2007). A non-marine depositional setting for the northern
466 Fortescue Group, Pilbara Craton, inferred from trace element geochemistry of stromatolitic carbonates.
467 *Precambrian Research*, *155*, 229–250. https://doi.org/10.1016/j.precamres.2007.02.002

468 Bourdet, J., & Pironon, J. (2008). Strain response and re-equilibration of $CH_4$-rich synthetic aqueous
469 fluid inclusions in calcite during pressure drops. *Geochimica et Cosmochimica Acta*, *72*, 2946–2959.
470 https://doi.org/10.1016/j.gca.2008.04.012

471 Bourdet, J., Eadington, P., Volk, H., George, S. C., Pironon, J., & Kempton, R. (2012). Chemical changes
472 of fluid inclusion oil trapped during the evolution of an oil reservoir: Jabiru-1A case study (Timor Sea,
473 Australia). *Marine and Petroleum Geology*, *36*, 118–139.
474 https://doi.org/10.1016/j.marpetgeo.2012.05.006

475 Braun, R. L., & Burnham, A. K. (1992). PMOD: A flexible model of oil and gas generation, cracking,
476 and expulsion. *Organic Geochemistry*, *19*, 161–172. https://doi.org/10.1016/0146-6380(92)90034-U

477 Chen, W., Lu, J., Jiang, S. Y., Ying, Y. C., & Liu, Y. S. (2018). Radiogenic Pb reservoir contributes to the
478 rare earth element (REE) enrichment in South Qinling carbonatites. *Chemical Geology*, *494*, 80–95.
479 https://doi.org/10.1016/j.chemgeo.2018.07.019

480 Coogan, L. A., Parrish, R. R., & Roberts, N. M. W. (2016). Early hydrothermal carbon uptake by the
481 upper oceanic crust: Insight from in situ U-Pb dating. *Geology*, *44*, 147–150.
482 https://doi.org/10.1130/G37212.1

Craig, H., & Gordon, L. (1965). Deuterium and oxygen-18 variations in the ocean and the marine atmosphere. In: Symposium on marine geochemistry. Graduate School of Oceanography, University of Rhode Island, OCC Publication No 3: 277.

Dyman, T. S., Spencer, C. W., Baird, J. K., Obuch, R. C., & Nielsen, D. T. (1997). Geologic and production characteristics of deep natural gas resources based on data from significant fields and reservoirs. *U.S. Geological Survey Bulletin*, 2146-C, 19–37.

Friedman, I., & O'Neil, J. R. (1977). Data of geochemistry: Compilation of stable isotope fractionation factors of geochemical interest. US Government Printing Office.

Frimmel, H. E. (2009). Trace element distribution in Neoproterozoic carbonates as palaeoenvironmental indicator. *Chemical Geology*, *258*, 338–353. https://doi.org/10.1016/j.chemgeo.2008.10.033

Fu, Q. (2019). Characterization and discrimination of paleokarst breccias and pseudobreccias in carbonate rocks: Insight from Ordovician strata in the northern Tarim Basin, China. *Sedimentary Geology*, *382*, 61–74. https://doi.org/10.1016/j.sedgeo.2019.01.007

Gao, J. F., & Zhou, M. F. (2013). Generation and evolution of siliceous high magnesium basaltic magmas in the formation of the Permian Huangshandong intrusion (Xinjiang, NW China). *Lithos*, *162–163*, 128–139. https://doi.org/10.1016/j.lithos.2013.01.002

Ge, X., Shen, C., Selby, D., Feely, M., & Zhu, G. (2020). Petroleum evolution within the Tarim Basin, northwestern China: Insights from organic geochemistry, fluid inclusions, and rhenium–osmium geochronology of the Halahatang oil field. *AAPG Bulletin*, *104*, 329–355. https://doi.org/10.1306/05091917253

503 Godeau, N., Deschamps, P., Guihou, A., Leonide, P., & Girard, J. P. (2018). U-Pb dating of calcite cement
504 and diagenetic history in microporous carbonate reservoirs: Case of the Urgonian Limestone, France.
505 *Geology*, *46*, 247–250. https://doi.org/10.1130/G39905.1

506 Goldstein, R. H., & Reynolds, T. J. (1994). Systematics of fluid inclusions in diagenetic minerals. SEPM
507 (Society for Sedimentary Geology) Short Course 31, pp. 1–199.

508 Han, C., Lin, C., Lu, X., Tian, J., Ren, L., & Ma, C. (2019). Petrological and geochemical constraints on
509 fluid types and formation mechanisms of the Ordovician carbonate reservoirs in Tahe Oilfield, Tarim
510 Basin, NW China. *Journal of Petroleum Science and Engineering*, *178*, 106–120.
511 https://doi.org/10.1016/j.petrol.2019.03.010

512 Haq, B. U., & Schutter, S. R. (2008). A chronology of Paleozoic sea-level changes. *Science*, *322*, 64–68.
513 https://doi.org/10.1126/science.1161648

514 Hays, P. D., & Grossman, E. L. (1991). Oxygen isotopes in meteoric calcite cements as indicators of
515 continental paleoclimate. *Geology*, *19*, 441–444. https://doi.org/10.1130/0091-
516 7613(1991)019<0441:OIIMCC>2.3.CO;2

517 Hyodo, A., Kozdon, R., Pollington, A. D., & Valley, J. W. (2014). Evolution of quartz cementation and
518 burial history of the Eau Claire Formation based on in situ oxygen isotope analysis of quartz
519 overgrowths. *Chemical Geology*, *384*, 168–180. https://doi.org/10.1016/j.chemgeo.2014.06.021

520 Jia, C., & Wei, G. (2002). Structural characteristics and petroliferous features of Tarim Basin. *Chinese*
521 *Science Bulletin*, *47*, 1–11. https://doi.org/10.1007/BF02902812

522 Kamber, B. S., & Webb, G. E. (2001). The geochemistry of late Archaean microbial carbonate:

523 Implications for ocean chemistry and continental erosion history. *Geochimica et Cosmochimica Acta*,
524 *65*, 2509–2525. https://doi.org/10.1016/S0016-7037(01)00613-5

525 Karlsen, D. A., Nedkvitne, T., Larter, S. R., & Bjørlykke, K. (1993). Hydrocarbon composition of
526 authigenic inclusions: Application to elucidation of petroleum reservoir filling history. *Geochimica et*
527 *Cosmochimica Acta*, *57*, 3641–3659. https://doi.org/10.1016/0016-7037(93)90146-N

528 Li, D., Liang, D., Jia, C., Wang, G., Wu, Q., & He, D. (1996). Hydrocarbon accumulations in the Tarim
529 Basin, China. *AAPG Bulletin*, *80*, 1587–1603. https://doi.org/10.1306/64EDA0BE-1724-11D7-
530 8645000102C1865D

531 Li, M., Wang, T., Chen, J., He, F., Yun, L., Akbar, S., & Zhang, W. (2010). Paleo-heat flow evolution of
532 the Tabei Uplift in Tarim Basin, northwest China. *Journal of Asian Earth Sciences*, *37*, 52–66.
533 https://doi.org/10.1016/j.jseaes.2009.07.007

534 Li, Q., Parrish, R. R., Horstwood, M. S. A., & Mcarthur, J. M. (2014). U-Pb dating of cements in
535 mesozoic ammonites. *Chemical Geology*, *376*, 76–83. https://doi.org/10.1016/j.chemgeo.2014.03.020

536 Liang, C., Cao, Y., Liu, K., Jiang, Z., Wu, J., & Hao, F. (2018). Diagenetic variation at the lamina scale
537 in lacustrine organic-rich shales: implications for hydrocarbon migration and accumulation.
538 *Geochimica et Cosmochimica Acta*, *229*, 112–128. https://doi.org/10.1016/j.gca.2018.03.017

539 Lin, C., Yang, H., Liu, J., Rui, Z., Cai, Z., & Zhu, Y. (2012). Distribution and erosion of the Paleozoic
540 tectonic unconformities in the Tarim Basin, Northwest China: Significance for the evolution of paleo-
541 uplifts and tectonic geography during deformation. *Journal of Asian Earth Sciences*, *46*, 1–
542 19. https://doi.org/10.1016/j.jseaes.2011.10.004

Liu, J., Li, Z., Cheng, L., & Li, J. (2017). Multiphase calcite cementation and fluids evolution of a deeply buried carbonate reservoir in the upper Ordovician Lianglitag Formation, Tahe Oilfield, Tarim Basin, NW China. *Geofluids*, 1–19. https://doi.org/10.1155/2017/4813235

Liu, Y., Qiu, N., Chang, J., Jia, J., Li, H., & Ma, A. (2020). Application of clumped isotope thermometry to thermal evolution of sedimentary basins: A case study of Shuntuoguole area in the Tarim Basin. *Chinese Journal of Geophysics (in Chinese)*, *63*, 597–611. https://doi.org/ 10.6038/cjg2020N0152

Lohmann, K. C. (1988). Geochemical patterns of meteoric diagenetic systems and their application to studies of paleokarst. In: James, N.P., Choquette, P.W. (Eds.), Paleokarst. Springer-Verlag, New York, pp. 58–80.

Mark, D. F., Green, P. F., Parnell, J., Kelley, S. P., Lee, M. R., & Sherlock, S. C. (2008). Late Palaeozoic hydrocarbon migration through the Clair field, West of Shetland, UK Atlantic margin. *Geochimica et Cosmochimica Acta*, *72*, 2510–2533. https://doi.org/10.1016/j.gca.2007.11.037

Mark, D. F., Parnell, J., Kelly, S. P, Lee, M. R., Sherlock, S. C., & Carr, A. (2005). Dating of multistage fluid flow in sandstones. *Science*, 309, 2048–2051. https://doi.org/10.1126/science.1116034

McArthur, J. M., Howarth, R. J., & Bailey, T. R. (2001). Strontium Isotope Stratigraphy: LOWESS Version 3: Best Fit to the Marine Sr-Isotope Curve for 0–509 Ma and Accompanying Look-up Table for Deriving Numerical Age. *Journal of Geology*, *109*, 155–170. https://doi.org/10.1086/319243

Mclennan, S. M. (2001). Relationships between the trace element composition of sedimentary rocks and upper continental crust. *Geochemistry Geophysics Geosystems*, *2*, 2000GC000109. https://doi.org/10.1029/2000GC000109

563 Moore, C. H., & Wade, W. J. (2013). Chapter 6 - Marine Diagenetic Environment. In: Moore, C. H., &
564 Wade, W. J. (Eds.). Carbonate Reservoir Porosity and Diagenesis in a Sequence Stratigraphic
565 Framework. Developments in Sedimentology (Elsevier), pp. 93–131.

566 Nothdurft, L. D., Webb, G. E., & Kamber, B. S. (2004). Rare earth element geochemistry of Late
567 Devonian reefal carbonates, Canning Basin, Western Australia: Confirmation of a seawater REE proxy
568 in ancient limestones. *Geochimica et Cosmochimica Acta*, *68*, 263–283.
569 https://doi.org/10.1016/S0016-7037(03)00422-8

570 Nuriel, P., Weinberger, R., Kylander-Clark, A. R. C., Hacker, B. R., & Craddock, J. P. (2017). The onset
571 of the Dead Sea transform based on calcite age-strain analyses. *Geology*, *45*, 587–590.
572 https://doi.org/10.1130/G38903.1

573 Pagel, M., Bonifacie, M., Schneider, D. A., Gautheron, C., Brigaud, B., Calmels D., et al. (2018).
574 Improving paleohydrological and diagenetic reconstructions in calcite veins and breccia of a
575 sedimentary basin by combining $\Delta_{47}$ temperature, $\delta^{18}$Owater and U-Pb age. *Chemical Geology*, *481*,
576 1–17. https://doi.org/10.1016/j.chemgeo.2017.12.026

577 Palmer, M. R., & Edmond, J. M. (1989). The strontium isotope budget of the modern ocean. *Earth*
578 *Planetary Science Letters*, *92*, 11–26. https://doi.org/10.1016/0012-821X(89)90017-4

579 Palmer, M. R., & Elderfield, H. (1985). Sr isotope composition of sea water over the past 75 Myr. *Nature*,
580 *314*, 526–528. https://doi.org/10.1038/314526a0

581 Pang, X., Tian, J., Pang, H., Xiang, C., Jiang, Z., & Li, S. (2010). Main progress and problems in research
582 on Ordovician hydrocarbon accumulation in the Tarim Basin. *Petroleum Science*, *7*, 147–163.
583 https://doi.org/10.1007/s12182-010-0022-z

584 Parnell, J. (1998). Introduction: Approaches to dating and duration of fluid flow and fluid-rock
585 introduction. In: Parnell, J. (Eds.). Dating and Duration of Fluid Flow and Fluid-Rock Interaction.
586 Geological Society of London Special Publications 144, pp. 1–8.

587 Paton, C., Hellstrom, J., Paul, B., Woodhead, J., & Hergt, J. (2011). Iolite: Freeware for the visualisation
588 and processing of mass spectrometric data. *Journal of Analytical Atomic Spectrometry*, *26*, 25082518.
589 https://doi.org/10.1039/C1JA10172B

590 Qiu, N., Chang, J., Zuo, Y., Wang, J., & Li, H. (2012). Thermal evolution and maturation of lower
591 Paleozoic source rocks in the Tarim Basin, northwest China. *AAPG Bulletin*, *96*, 789–821.
592 https://doi.org/10.1306/09071111029

593 Ramos, F. C., Wolff, J. A., & Tollstrup, D. L. (2004). Measuring 87Sr/86Sr variations in minerals and
594 groundmass from basalts using LA-MC-ICPMS. *Chemical Geology*, *211*, 135–158.
595 https://doi.org/10.1016/j.chemgeo.2004.06.025

596 Roberts, N. M. W., & Walker, R. J. (2016). U-Pb geochronology of calcite-mineralized faults: Absolute
597 timing of rift-related fault events on the northeast Atlantic margin. *Geology*, *44*, 531–534.
598 https://doi.org/10.1130/G37868.1

599 Roberts, N. M. W., Drost, K., Horstwood, M. S., Condon, D. J., Chew, D., Drake, H., et al. (2020). Laser
600 ablation inductively coupled plasma mass spectrometry (LA-ICP-MS) U–Pb carbonate geochronology:
601 strategies, progress, and limitations. *Geochronology*, *2*, 33–61. https://doi.org/10.5194/gchron-2-33-
602 2020

603 Roberts, N. M. W., Rasbury, E. T., Parrish, R. R., Smith, C. J., Horstwood, M. S., & Condon, D. J. (2017).
604 A calcite reference material for LA-ICP-MS U-Pb geochronology. *Geochemistry Geophysics*

605 *Geosystems*, *18*, 2807–2814. https://doi.org/10.1002/2016GC006784

606 Robinson, B. W., & Gunatilaka, A. (1991). Stable isotope studies and the hydrological regime of sabkhas
607 in southern Kuwait, Arabian Gulf. *Sedimentary Geology*, *73*, 141–159. https://doi.org/10.1016/0037-
608 0738(91)90027-B

609 Schmidt, M., Xeflide, S., Botz, R., & Mann, S. (2005). Oxygen isotope fractionation during synthesis of
610 CaMg-carbonate and implications for sedimentary dolomite formation. *Geochimica et Cosmochimica*
611 *Acta*, *69*, 4665–4674. https://doi.org/10.1016/j.gca.2005.06.025

612 Seewald, J. S. (1994). Evidence for metastable equilibrium between hydrocarbons under hydrothermal
613 conditions. *Nature*, *370*, 285–285. https://doi.org/10.1038/370285a0

614 Shields, G. A., & Webb, G. E. (2004). Has the REE composition of seawater changed over geological
615 time? *Chemical Geology*, *204*, 103–107. https://doi.org/10.1016/j.chemgeo.2003.09.010

616 Tang, Y., Cui, K., Zheng, Z., Gao, J., Han, J., Yang, J., & Liu, L. (2020). LA-ICP-MS U–Pb
617 geochronology of wolframite by combining NIST series and common lead-bearing MTM as the
618 primary reference material: Implications for metallogenesis of South China. *Gondwana Research*, *83*,
619 217–231. https://doi.org/10.1016/j.gr.2020.02.006

620 Van Kranendonk, M. J., Webb, G. E., & Kamber, B. S. (2003). Geological and trace element evidence
621 for a marine sedimentary environment of deposition and biogenicity of 3.45 Ga stromatolitic
622 carbonates in the Pilbara Craton, and support for a reducing Archaean ocean. *Geobiology*, *1*, 91–108.
623 https://doi.org/10.1046/j.1472-4669.2003.00014.x

624 Vermeesch, P. (2018). IsoplotR: A free and open toolbox for geochronology. *Geoscience Frontiers*, *9*,

1479–1493. https://doi.org/10.1016/j.gsf.2018.04.001

Wang, T., Dai, S., Li, M., Zhang, W., Qiu, N., & Wang, G. (2010). Stratigraphic thermohistory and its implications for regional geoevolution in the Tarim Basin, NW China. *Science China Earth Sciences*, *53*, 1495–1505. https://doi.org/10.1007/s11430-010-4069-x

Webb, G. E., & Kamber, B. S. (2000). Rare earth elements in Holocene reefal microbialites: A new shallow seawater proxy. *Geochimica et Cosmochimica Acta*, *64*, 1557–1565. https://doi.org/10.1016/S0016-7037(99)00400-7

Wu, Q., Fu, H., Huang, H., Zuo, Y., & Lu, R. (2008). Sedimentary evolution of the Lower Carboniferous Bachu Formation in the Tarim River area, Xinjiang. *Sedimentary Geology and Tethyan Geology*, *28*, 79–83. https://doi.org/10.3969/j.issn.1009-3850.2008.03.014

Xu, Q., Qiu, N., Liu, W., & Chang, Q. (2019). Reconstructing the basin thermal history with clumped isotope (in Chinese). *Chinese Science Bulletin*, *64*, 566–578. https://doi.org/10.1360/N972018-00458

Yang, P., & Liu, K. (2020). Fluid inclusion re-equilibration in carbonate rock caused by freezing during microthermometric analysis. *Acta Geologica Sinica-English Edition*, *94*, 580–582. https://doi.org/10.1111/1755-6724.14524

Zhang, S., & Huang, H. (2005). Geochemistry of Palaeozoic marine petroleum from the Tarim Basin, NW China: Part 1. Oil family classification. *Organic Geochemistry*, *36*, 1204–1214. https://doi.org/10.1016/j.orggeochem.2005.01.013

Zhang, Y., & Luo, X. (2011). K-Ar dating of authigenic illites and hydrocarbon accumulation history of the Silurian bituminous sandstone reservoirs in Yingmaili area, Tarim Basin. *Petroleum Exploration*

645 *and Development*, *38*, 203–210.

646 Zhang, Z., Zhu, G., Zhang, Y., Han, J., Li, T., Wang, E., & Greenwood, P. (2018). The origin and
647 accumulation of multi-phase reservoirs in the east Tabei uplift, Tarim Basin, China. *Marine and*
648 *Petroleum Geology*, *98*, 533–553. https://doi.org/10.1016/j.marpetgeo.2018.08.036

649 Zhao, Y. Y, & Zheng, Y. F. (2013). Geochemical constraints on the origin of post-depositional fluids in
650 sedimentary carbonates of the Ediacaran system in South China. *Precambrian Research*, *224*, 341–
651 363. https://doi.org/10.1016/j.precamres.2012.10.014

652 Zhu, G., Zhang, S., Liu, K., Yang, H., Zhang, B., Su, J., & Zhang, Y. (2013). A well-preserved 250
653 million-year-old oil accumulation in the Tarim Basin, western China: Implications for hydrocarbon
654 exploration in old and deep basins. *Marine and Petroleum Geology*, *43*, 478–488.
655 https://doi.org/10.1016/j.marpetgeo.2012.12.001

656 Zhu, G., Zhang, S., Su, J., Zhang, B., Yang, H., Zhu, Y., & Gu, L. (2013). Alteration and multi-stage
657 accumulation of oil and gas in the Ordovician of the Tabei Uplift, Tarim Basin, NW China:
658 Implications for genetic origin of the diverse hydrocarbons. *Marine and Petroleum Geology*, *46*, 234–
659 250. https://doi.org/10.1016/j.marpetgeo.2013.06.007

660 Zhu, G., Zhang, Z., Zhou, X., Li, T., Han, J., & Sun, C. (2019). The complexity, secondary geochemical
661 process, genetic mechanism and distribution prediction of deep marine oil and gas in the Tarim Basin,
662 China. *Earth-Science Reviews*, *198*, 102930. https://doi.org/10.1016/j.earscirev.2019.102930

## 663 References from Supporting Information

664 Ludwig, K. R. (1999). On the treatment of concordant uranium-lead ages. *Geochimica et Cosmochimica*

665 *Acta*, *62*, 665–676. https://doi.org/10.1016/S0016-7037(98)00059-3

666 Vermeesch, P. (2018). IsoplotR: A free and open toolbox for geochronology. *Geoscience Frontiers*, *9*,

667 1479–1493. https://doi.org/10.1016/j.gsf.2018.04.001

668

## Table and Figure Captions

**Figure 1.** (a) Stratigraphic and structural cross section of the Tabei Uplift, Tarim Basin showing the location of the reservoir sample (star). Inset shows the geographic location of the Tabei Uplift; (b) Generalized stratigraphic column of Well TK721, showing the depths of various stratal boundaries and the position of the sample studied in this study.

**Figure 2.** Photomicrographs of calcite vein showing the paragenetic relationships of calcite cements, the occurrence of "dust rim", bitumen, and oil inclusions in the Ordovician Yingshan Formation ($O_{1\text{-}2}y$). (a) and (b) Photomicrograph mosaics of the calcite vein studied under transmitted light and CL, showing five generations of cement (C1 to C5), HR = host rock, B = bitumen, DR = dust rim; (c) BS-SEM image showing fine-grained detrital quartz (Q) grains filling the "dust rim" between C1 and C2 calcite cements; (d) Photomicrograph showing dissolution of C3 and the presence of bitumen (B); (e) Fluorescence photomicrograph showing bitumen (B) rims between C1 and C4, C4 and C5; (f) Fluorescence photomicrograph showing yellow-orange oil inclusions along an annealed microfracture in C3; (g) and (h) Close-up view of photomicrographs under transmitted light and UV fluorescence showing bitumen (B) and oil inclusions along the C1 and C4 contact.

**Figure 3.** Fluid inclusion characteristics within the calcite vein in the Ordovician Yingshan Formation ($O_{1\text{-}2y}$). (a) Cross plot of fluid inclusion salinity vs homogenization temperatures (Th) for the C1-C5 calcite cements, ISW = initial seawater, PFW = present-day formation water. Note that the black solid lines represent the fluid evolution paths of the carbonate reservoir during the Carboniferous, while the gray dotted line represents the inferred fluid evolution path; (b) Histogram of homogenization temperatures (Th) of oil inclusions, showing a confined distribution with a mode of 65–70 °C. Inset

690 shows fluorescence spectra of individual oil inclusions from the calcite vein, showing a consistent
691 spectral peak around 655 nm.

692 **Figure 4.** REE + Y characteristics for the C1 to C5 calcite cements and host rock in the Ordovician
693 Yingshan Formation ($O_{1-2}y$). (a)-(e) PAAS-normalized REE + Y patterns for the calcite vein and host
694 rock; (f) Comparison of various REE ratios among various generations of calcite vein and host rock.
695 Note that A-H denote the median of [Pr/Yb], [Pr/Tb], [Tb/Yb], [La/La*], [Ce/Ce*], [Gd/Gd*], [Er/Er*]
696 and [Eu/Eu*] ratios relative to the PAAS-normalization, respectively.

697 **Figure 5.** Carbon, oxygen and strontium isotope characteristics for the C1-C5 calcite cements and host
698 rock studied in the Ordovician Yingshan Formation ($O_{1-2}y$).

699 **Figure 6.** (a)-(f) U-Pb Tera-Wasserburg concordia plots for the C1-C5 calcite cements and host rock in
700 the Ordovician Yingshan Formation ($O_{1-2}y$). The results are reported as t ± x | y | z, where t stands for the
701 age or initial Pb-ratio, x is the standard error, y and z are the (95%) confidence intervals without and with
702 over-dispersion, respectively.

703 **Figure 7.** Schematic diagram showing the fluid-flow events and formation processes of the C1-C5
704 calcite cements during the Carboniferous. Insert shows burial history diagram of the studied Ordovician
705 reservoir for comparison (modified from Liu et al., 2017), depicting the relative burial depths of the
706 calcite cement precipitated.

707 **Figure 8.** Schematic diagrams illustrating fluid evolution history in the studied Ordovician carbonate
708 reservoir during the Carboniferous. (a) Hyper-saline brine intrusion from the lagoon during the
709 precipitation of C1; (b) Influx of meteoric water into the reservoir during C2 and C3 precipitation; (c)
710 Petroleum charge occurring during the cementation of C4; (d) Reservoir formation water in equilibrium

711 with the Ordovician connate water during the precipitation of C5.

712 **Table 1** Electron Microprobe Analysis (EMPA) of major elements for the C1-C5 calcite cements and

713 host rock studied in the Ordovician Yingshan Formation ($O_{1-2}y$).

714 **Table 2** Summary of rare earth element compositions for the C1-C5 calcite cements and host rock

715 studied.

716 **Table 3** Carbon and oxygen and strontium isotope ratios for the C1-C5 calcite cements and host rock

717 studied.

718

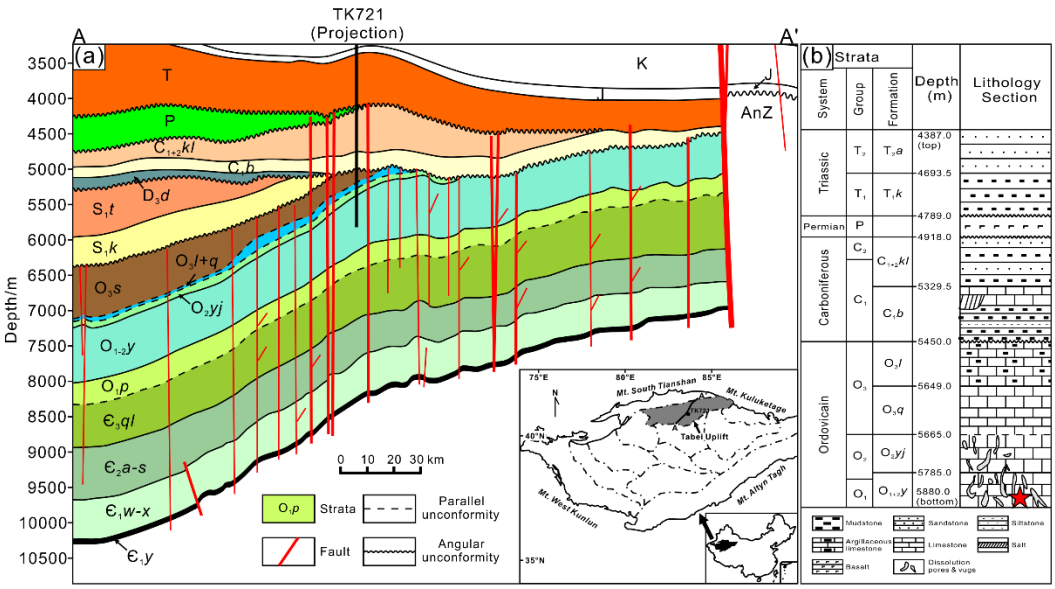


**Figure 1.** (a) Stratigraphic and structural cross section of the Tabei Uplift, Tarim Basin. Inset shows the geographic location of the Tabei Uplift; (b) Generalized stratigraphic column of Well TK721, showing the depths of various stratal boundaries and the position of the sample (red star) studied in this study.

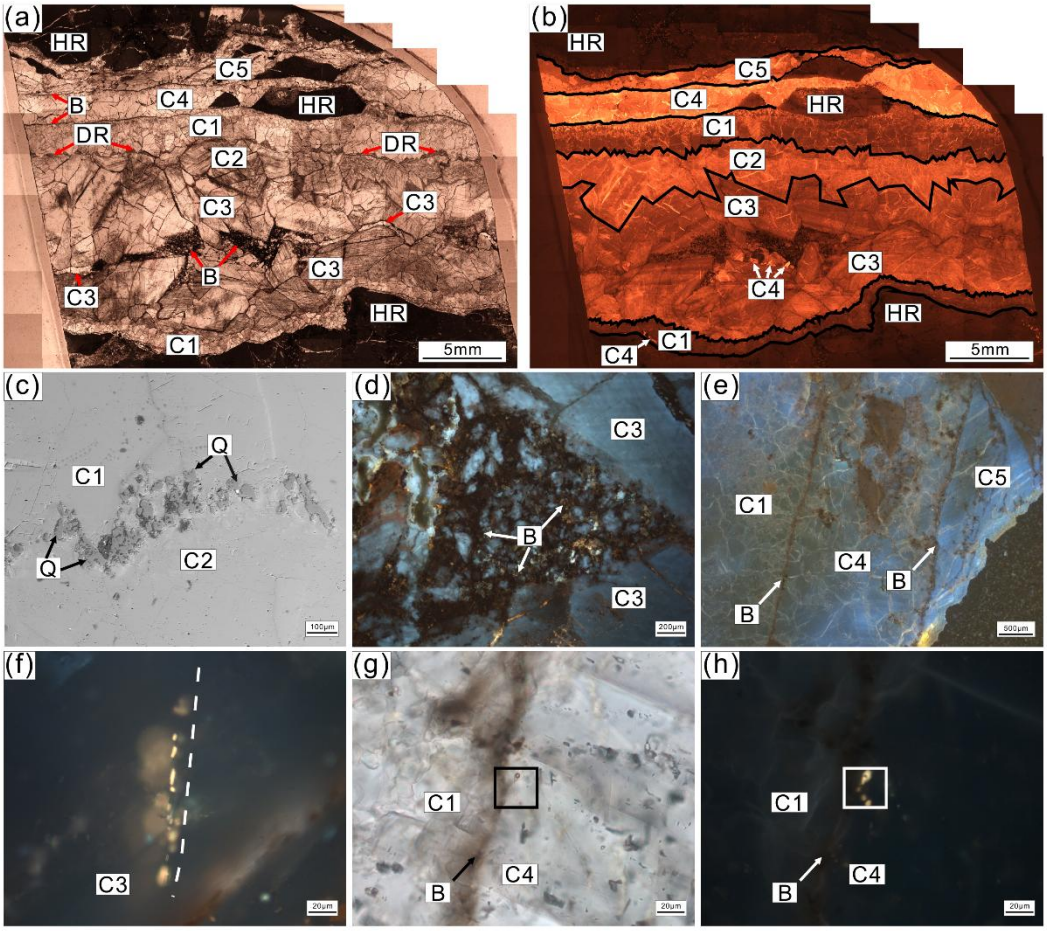


**Figure 2.** Photomicrographs of calcite vein showing the paragenetic relationships of calcite cements, the occurrence of "dust rim", bitumen, and oil inclusions in the Ordovician Yingshan Formation ($O_{1-2}y$). (a) and (b) Photomicrograph mosaics of the calcite vein studied under transmitted light and CL, showing five generations of cement (C1 to C5), HR = host rock, B = bitumen, DR = dust rim; (c) BS-SEM image showing fine-grained detrital quartz (Q) grains filling the "dust rim" between C1 and C2 calcite cements; (d) Photomicrograph showing dissolution of C3 and the presence of bitumen (B); (e) Fluorescence photomicrograph showing bitumen (B) rims between C1 and C4, C4 and C5; (f) Fluorescence photomicrograph showing yellow-orange oil inclusions along an annealed microfracture in C3; (g) and (h) Close-up view of photomicrographs under transmitted light and UV fluorescence showing bitumen (B) and oil inclusions along the C1 and C4 contact.

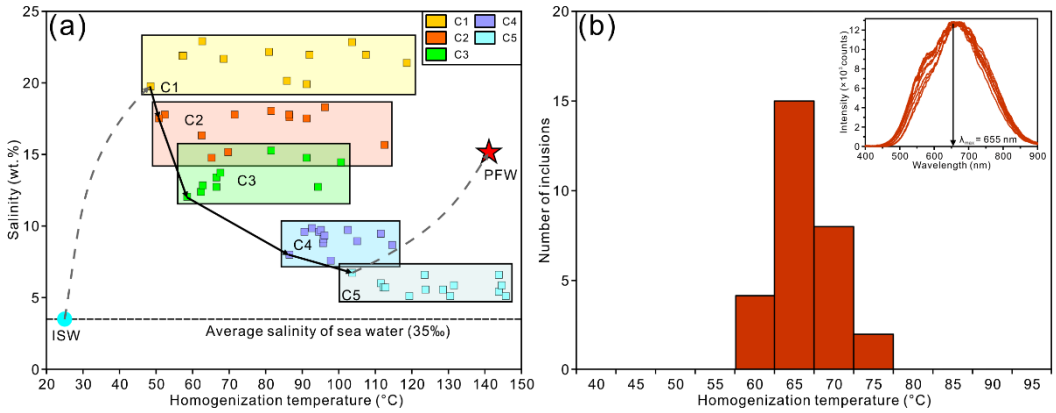


**Figure 3.** Fluid inclusion characteristics within the calcite vein in the Ordovician Yingshan Formation ($O_{1\text{-}2}y$). (a) Cross plot of fluid inclusion salinity vs homogenization temperatures (Th) for the C1-C5 calcite cements, ISW = initial seawater, PFW = present-day formation water. Note that the black solid lines represent the fluid evolution paths of the carbonate reservoir during the Carboniferous, while the gray dotted line represents the inferred fluid evolution path; (b) Histogram of homogenization temperatures (Th) of oil inclusions, showing a confined distribution with a mode of 65–70 ℃. Inset shows fluorescence spectra of individual oil inclusions from the calcite vein, showing a consistent spectral peak around 655 nm.

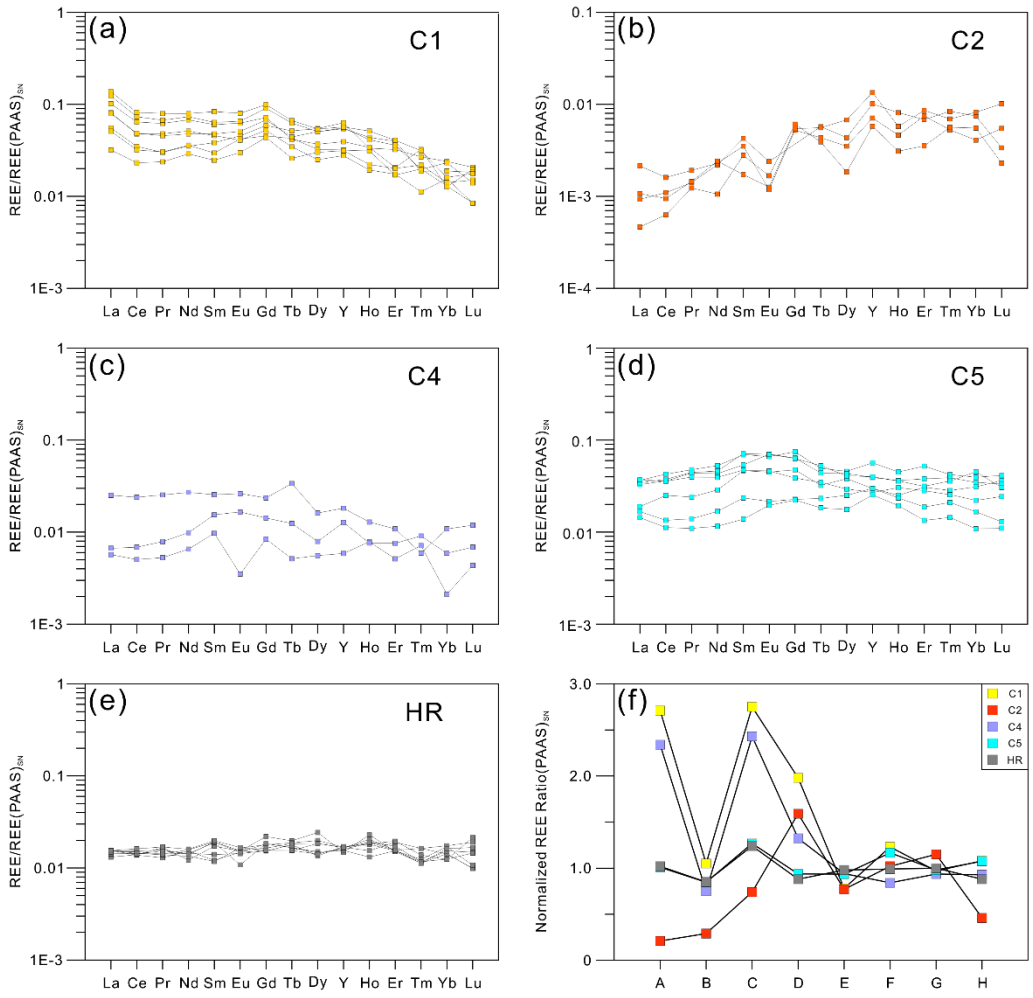


**Figure 4.** REE + Y characteristics for the C1 to C5 calcite cements and host rock in the Ordovician Yingshan Formation ($O_{1\text{-}2}y$). (a)-(e) PAAS-normalized REE + Y patterns for the calcite vein and host rock; (f) Comparison of various REE ratios among various generations of calcite vein and host rock. Note that A-H denote the median of [Pr/Yb], [Pr/Tb], [Tb/Yb], [La/La*], [Ce/Ce*], [Gd/Gd*], [Er/Er*] and [Eu/Eu*] ratios relative to the PAAS-normalization, respectively.

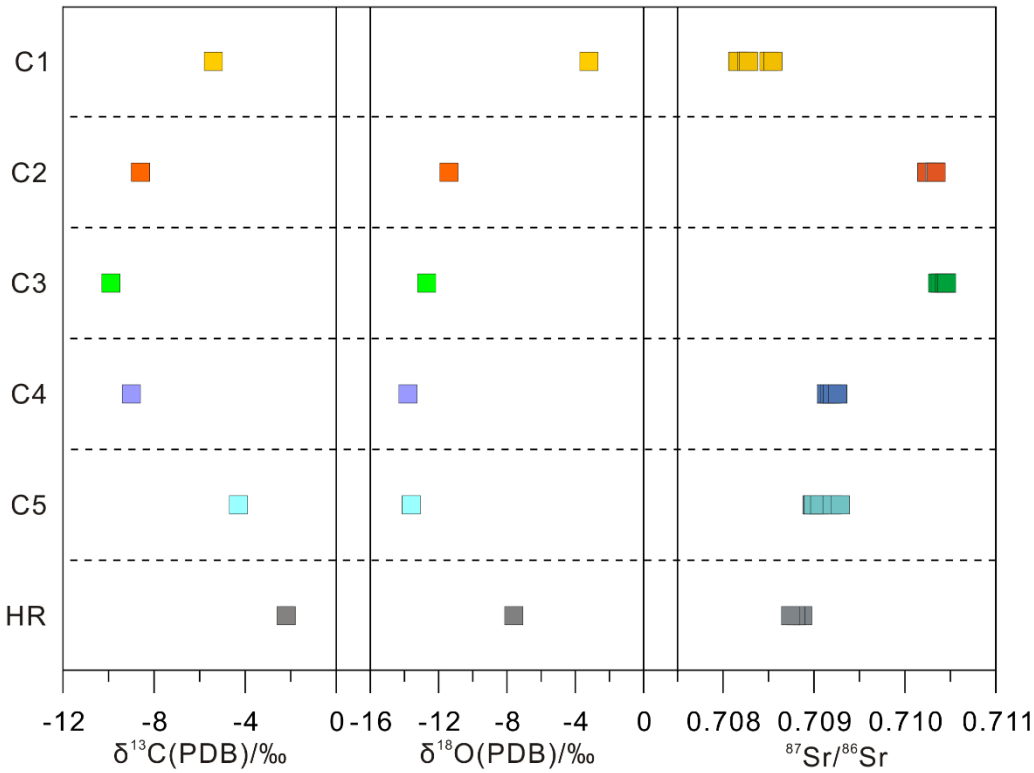


**Figure 5.** Carbon (C), oxygen (O) and strontium (Sr) isotope characteristics for the C1-C5 calcite cements and host rock in the Ordovician Yingshan Formation ($O_{1\text{-}2}y$).

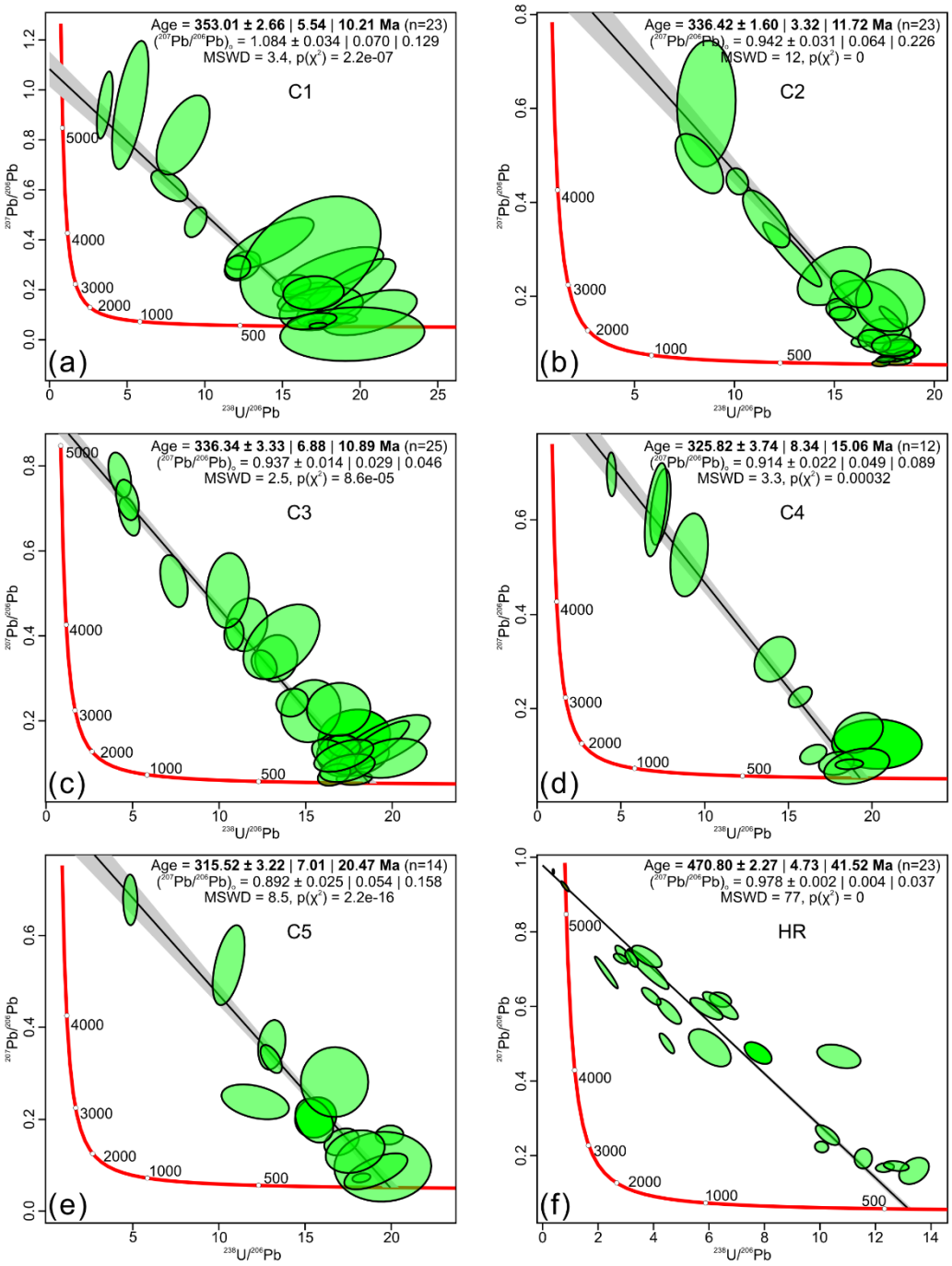


**Figure 6.** (a)-(f) U-Pb Tera-Wasserburg concordia plots for the C1-C5 calcite cements and host rock in the Ordovician Yingshan Formation ($O_{1\text{-}2}y$). The results are reported as t ± x | y | z, where t stands for the age or initial Pb-ratio, x is the standard error, y and z are the (95%) confidence intervals without and with over-dispersion, respectively.

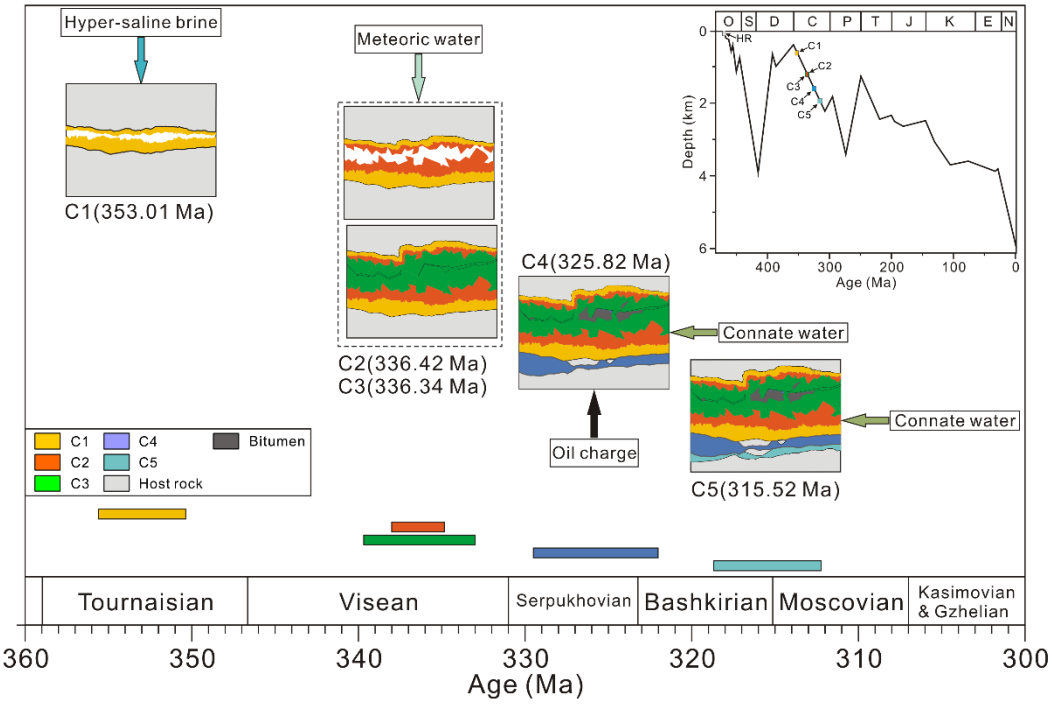


**Figure 7.** Schematic diagram showing the fluid-flow events and formation processes of the C1-C5 calcite cements during the Carboniferous. Insert shows burial history diagram of the studied Ordovician reservoir for comparison (modified from Liu et al., 2017), depicting the relative burial depths of the calcite cement precipitated.

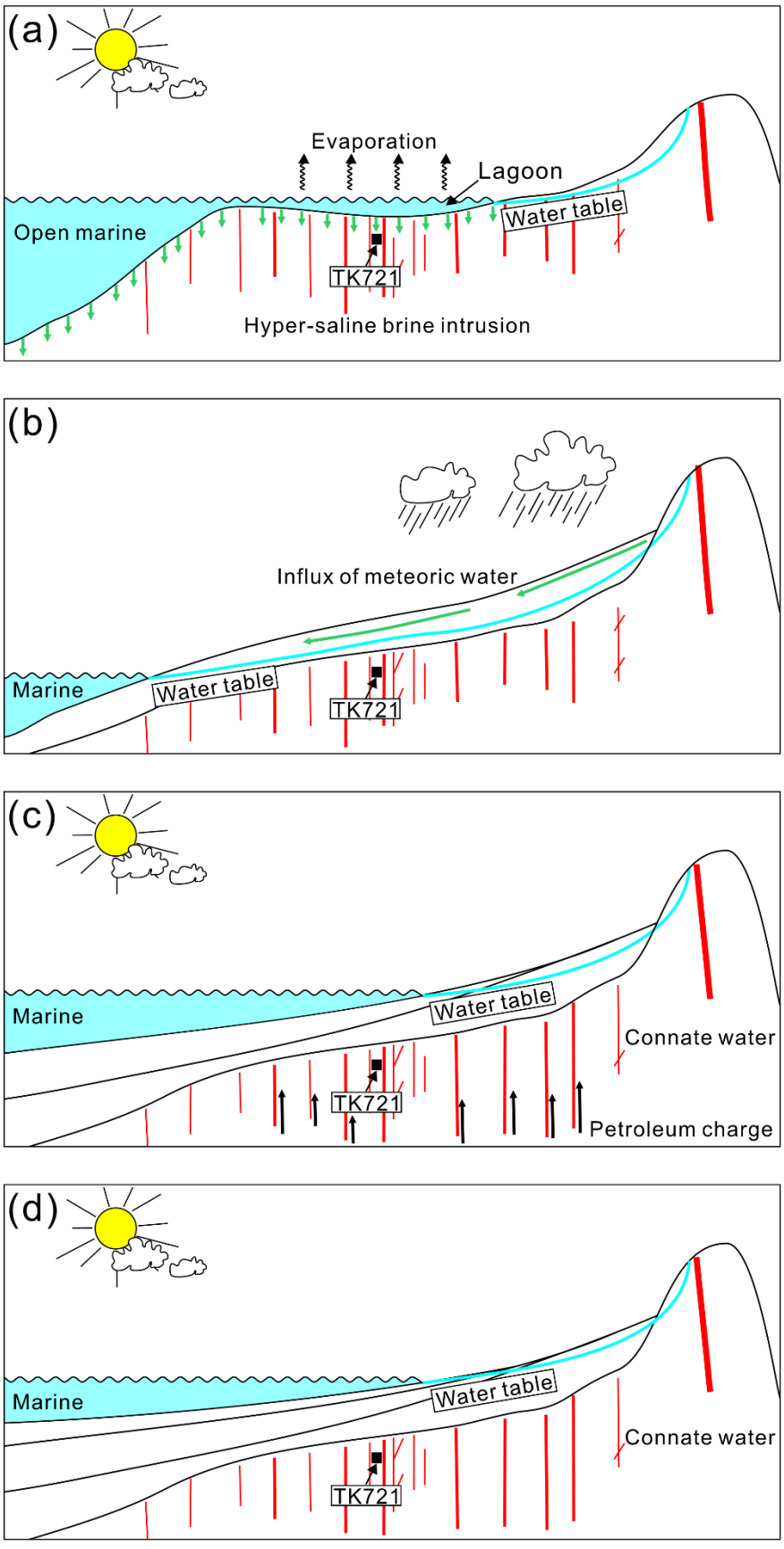


**Figure 8.** Schematic diagrams illustrating fluid evolution history in the studied Ordovician carbonate

reservoir during the Carboniferous. (a) Hyper-saline brine intrusion from the lagoon during the precipitation of C1; (b) Influx of meteoric water into the reservoir during C2 and C3 precipitation; (c) Petroleum charge occurring during the cementation of C4; (d) Reservoir formation water in equilibrium with the Ordovician connate water during the precipitation of C5.